Effects of PMMA-transfer residues on the growth of organic semiconductor molecules on CVD graphene

Markus Kratzer,[1,#,*] Bernhard C. Bayer,[2,3,#] Piran R. Kidambi,[2,4] Aleksandar Matković,[5] Radoš Gajić,[5] Andrea Cabrero-Vilatela,[2] Robert S. Weatherup,[2] Stephan Hofmann[2] and Christian Teichert[1]

[1]*Institute of Physics, Montanuniversitaet Leoben, A 8700, Leoben, Austria*

[2]*Department of Engineering, University of Cambridge, Cambridge, CB3 0FA, United Kingdom*

[3]*Faculty of Physics, University of Vienna, Boltzmanngasse 5, A 1090, Vienna, Austria*

[4]*Department of Mechanical Engineering, Massachusetts Institute of Technology, Cambridge, 02139, Massachusetts, USA*

[5]*Institute of Physics, University of Belgrade, 11080 Belgrade, Serbia*

[#]*Equally contributed*

[*]*Corresponding author*

Abstract

Scalably grown and transferred graphene is a highly promising material for organic electronic applications, but controlled interfacing of graphene thereby remains a key challenge. Here, we study the growth characteristics of the important organic semiconductor molecule para-hexaphenyl (6P) on chemical vapor deposited (CVD) graphene that has been transferred with polymethylmethacrylate (PMMA) onto oxidized Si wafer supports. A particular focus is on the influence of PMMA residual contamination, which we systematically reduce by H_2 annealing prior to 6P deposition. We find that 6P grows in a flat-lying needle-type morphology, surprisingly independent of the level of PMMA residue and of graphene defects. Wrinkles in the graphene typically act as preferential nucleation centers. Residual PMMA does however limit the length of the resulting 6P needles by restricting molecular diffusion/attachment. We discuss the implications for organic device fabrication, with particular regard to contamination and defect tolerance.

Article Text

Graphene is a highly promising material for future organic semiconductor device applications due to its unique combination of properties including high carrier mobility, high optical transmittance, chemical inertness and high mechanical strength and flexibility. Numerous device concepts have been reported,[1–8] many of which utilize graphene as a transparent, conductive electrode material in contact with organic semiconductor layers. In this context, the growth modes of the organic molecules on the graphene have a key impact on the organics' (opto-)electronic properties.[2,9–31]

While a lot of progress has been made on scalable graphene manufacture in particular based on chemical vapor deposition (CVD),[32,33] controlled transfer and interfacing of graphene remains a key challenge. Graphene layer transfer often involves the use of polymer support, typically polymethylmethacrylate (PMMA), which is challenging to subsequently remove from the graphene.[34–42] Similar residues arise from lithographic patterning of graphene using resist layers.[43–45] Technologically relevant, large area CVD graphene is poly-crystalline with a range of inherent defects, and upon transfer mono- and few-layer graphene tends to wrinkle.[28] Despite their potentially crucial impact on organic device performance, the detailed effects of polymer residue, graphene defects, and wrinkles on subsequent organic semiconductor device layer nucleation and growth remain largely unknown.

Here, we investigate the effect of scalable CVD mono-layer graphene (MLG) transfer processes (using PMMA) on the growth characteristics of the important, blue-light-emitting organic semiconductor molecule para-hexaphenyl (6P, also called para-sexiphenyl).[9–14,46–58] We find that 6P grows in a flat-lying needle-type morphology on CVD MLG transferred to oxidized Si wafers, irrespective of observed PMMA residue levels and MLG defects. This indicates that MLG dominates interface properties even in the case of severe contamination or damage. Preferential 6P nucleation at MLG wrinkles is observed.[10] While residual PMMA does not change the growth morphology of the 6P it severely limits the length of the resulting 6P needles by hindering molecular diffusion/attachment. Only subsequent to post-transfer H_2 anneals that remove even minor PMMA residues, is extended 6P needle growth obtained which resembles that observed on clean exfoliated MLG.[12–14]

We grow MLG by low-pressure CVD on Cu catalysts.[32,33] The as-grown MLG on the Cu is then covered with a PMMA layer and wet chemical etches are used to release the PMMA-coated MLG from the Cu to subsequently transfer the stack onto SiO_2 (300 nm) covered Si-wafers. We chose SiO_2 as the support due to its widespread use as a model dielectric surface.[43] After transfer, the PMMA layer is initially removed by acetone followed by isopropanol. For selected samples, additional cleaning from PMMA residues is subsequently done by low-pressure (1 mbar) anneals in H_2 at temperatures up to 500 °C (typical annealing time 3 hours). 6P is then deposited onto the transferred CVD MLG via hot wall epitaxy (HWE) with MLG substrates held at 90 °C (deposition time 5 min).[12,13] For further experimental details see Supporting Information.[59]

The small conjugated 6P molecule is chosen as a model system since its growth behavior is highly sensitive to surface conditions, showing two principal growth morphologies[50,52–55,57,58] (Figure 1): Flat-lying "needle" growth (molecular long axis roughly parallel to the substrate surface and normal to the needle's long axis) is preferred on crystalline substrates whereas upright "island" growth (molecular long axis roughly perpendicular to the substrate surface) prevails on amorphous surfaces including SiO_2.[12,60] Control over these growth morphologies is of key importance for device applications as needle- or island morphologies strongly influence opto-electronic properties of 6P layers.[46] 6P needles characteristically show a high lateral aspect ratio and commonly exhibit heights of tens of nm, as multiple flat-lying 6P layers stack (in herringbone arrangement, see Figure 1) in the needles. In contrast, upright 6P islands form terraced mounds with discrete heights corresponding to multiples of the 6P length of ~2.7 nm.[50] At low coverages usually only mono- or bi-layer islands exist, resulting in comparably small island heights of only ~2.0 nm - 5.3 nm (depending on small 6P tilt).[50,58] This difference in height and morphology makes it straightforward to differentiate needle and island 6P growth based on atomic force microscopy (AFM, see insets in Figure 1). Previous work on 6P deposition on ultra-high-vacuum-grown[9–11] and exfoliated MLG[12–14] demonstrated that for these clean MLG interfaces 6P grows exclusively in the flat-lying needle-type mode under our HWE conditions at 90 °C. The flat-lying needle morphology is commonly ascribed to strong π-π interactions between 6P's organic backbone and MLG's sp^2 lattice.[61]

Figure 2 shows a series of AFM topography images of 6P morphologies on PMMA-transferred CVD MLG, starting with as transferred MLG and for samples which were post-transfer cleaned by H_2 annealing at increasing temperatures (280 °C to 500 °C) prior to 6P deposition. Only needle-type 6P growth is observed on the CVD MLG, irrespective of H_2 annealing treatment. Strikingly however, with increasing annealing temperature the needle length increases while the needle areal density reduces. In general, 6P needles nucleate preferentially at the CVD graphene wrinkles[9,11,28] and typically extend roughly perpendicular to the wrinkle direction. For the MLG which was H_2-treated between 280 °C to 350 °C, needles also nucleate at lump-like features which we attribute to accumulated PMMA residues (see below). For further increased annealing temperatures of 400 °C and 500 °C, the longer 6P needles frequently act as nucleation centers themselves yielding the formation of cross or star like needle bunches, similar to 6P deposition on exfoliated MLG.[12,13]

Figure 3a shows a quantitative analysis of 6P needle length distributions as a function of MLG H_2 annealing temperature. For each histogram the lengths of 250-500 needles were evaluated. Figure 3b shows the average needle length extracted from the histograms. The non-H_2-annealed, as-transferred sample exhibits the shortest average needle length, the narrowest distribution and also the shortest maximum needle length (<0.5 µm). With increasing annealing temperature, the average needle lengths increase and concurrently the distributions broaden asymmetrically towards larger maximum needle lengths. We note, however, that also the H_2 annealed samples continue to feature a significant number of needles shorter than 0.5 µm. For 500 °C, where the largest needle lengths are reached, the distribution becomes bimodal: A high number of very short needles (< 150 nm), nucleating at the MLG wrinkles (albeit covering only just over 1% of the surface) can be found in addition to long needles that reach lengths of over 1.5 µm. While we observe an increase in needle length with H_2 annealing temperature, conversely the 6P needle areal density decreases from ~4.0 μm^{-2} (as transferred) to ~1.5 μm^{-2} (annealed at 500 °C after transfer). Typical 6P needle heights and widths range from 20-40 nm and 50-200 nm, respectively.

We conclude that 6P grows on CVD graphene in a flat-lying needle-like fashion irrespective of the PMMA residue cleaning procedure applied but that the length and density of the resulting 6P needles is strongly dependent on the PMMA removal process prior to 6P deposition.

To understand the origin of these dependencies, we investigate the state of the CVD MLG at the point of 6P nucleation. Figure 4a shows AFM images of as transferred and H_2-annealed CVD MLG before 6P deposition. The non-H_2-annealed, as transferred sample exhibits a high density of up to 1 nm high features evenly distributed over the surface, which are ascribed to PMMA residues, in agreement with previous observations on only acetone/isopropanol cleaned transferred CVD MLG.[36] H_2 annealing at 280 °C results in a noticeably reduced surface roughness (root-mean-square, RMS) from 0.8 nm (as transferred) to 0.5 nm (280 °C) in the MLG areas between wrinkles, indicative of the onset of PMMA removal.[34,36] Further increase of the H_2 treatment temperature successively reduces the surface roughness (down to RMS ~0.3 nm for 500 °C) which is attributed to the removal of PMMA residues from the MLG basal planes, with only few isolated larger PMMA residues remaining. Figure 4b further quantifies this trend of increasing PMMA removal with increasing H_2 annealing temperature by plotting the relative volume, relative coverage and average thickness of the PMMA residues as a function of the H_2 annealing temperature. From as deposited to 280 °C the PMMA residue reduces in average thickness (in agreement with the RMS roughness decrease from 0.8 nm to 0.5 nm), but the lateral relative coverage remains fairly constant. Comparison of Figure 4a and the relative coverage values however indicates that during 280 °C annealing the PMMA residues are also spatially redistributed such that larger continuous MLG areas become available for 6P needle growth, thus resulting in the observed 6P needle length increase (Figures 2 and 3). For further increased annealing temperatures (350 °C, 500 °C) the PMMA residue reduces in relative volume, relative coverage and average thickness, in agreement with the visual impression from Figure 4a and the RMS roughness decrease to 0.3 nm.

While increasing H_2 treatment temperatures thus result in more efficient PMMA removal, concurrently alterations to the graphene quality occur, as evidenced by Raman spectroscopy (Figure 4c). The intensity ratio of the 2D/G peaks drops with increasing annealing temperature from ~2.3 (as-transferred) to ~0.7 (500 °C), indicative for a change in the graphene doping level and partly consistent with PMMA removal but also with defect formation in MLG.[36,38,62] The defect-related D peak starts to rise for 350 °C annealing and emerges notably at 500 °C. This indicates minor generation of defects up to annealing temperatures of ~350 °C and pronounced damage to the MLG for higher annealing temperatures. This means that, while high

temperature H_2 annealing efficiently removes PMMA and thereby enables extended 6P needle growth, it also damages the underlying MLG.

To understand how the PMMA residues influence 6P growth, we compare 6P morphologies on selected reference substrates in Figure 5. 6P is deposited onto (a) exfoliated MLG, (b) spin-coated homogeneous PMMA layers, and (c) filtered-cathodic-vacuum-arc deposited amorphous carbon (a-C) films[63] (all on SiO_2 covered Si wafers). The exfoliated MLG serves as a clean and defect-free ideal graphene surface, while the PMMA layer and the a-C film represent "dirty" and fully defective graphene, respectively (Raman spectrum of a-C in Supporting Figure S4[59]). We find flat-lying needle growth on the exfoliated MLG (consistent with previous literature[12–14]) but interestingly a drastic change to upright 6P island growth on both the PMMA layer and the defective a-C.[53,54] The 6P island growth on the reference PMMA layer indicates that for extended PMMA residues on MLG, a change to island-type 6P growth would occur. Similarly, the reference a-C result suggests that for high defect levels in MLG a change-over from 6P needle to island growth is to be expected. Equally, in the extreme case when CVD MLG would be so strongly pitted that the bare SiO_2 substrate underneath would be exposed also 6P island growth would be expected, as 6P is well known from literature to generally show island-type morphology on bare SiO_2.[12,60] In Figure 2 however no upright 6P island-type growth is observed on the CVD MLG irrespective of the PMMA residue and the MLG defect levels revealed in Figure 4. This indicates that the observed PMMA residuals on the MLG (even without H_2 annealing) do not provide large enough interaction to induce island growth with upright molecule orientation. Thus, 6P growth appears to still be dominated by the π-π interactions between the 6P organic backbone and the sp^2 MLG lattice, even for the relatively contaminated MLG. This surprising resilience of the underlying MLG to dominate the interface properties, even in the case of the observed severe contamination, may be a key technological advantage of MLG. Similarly, despite the comparably high defect levels in the Raman data for high temperature H_2 annealed MLG (Figure 4c), also in this defective MLG the sp^2 lattice still appears to dominate as a template to promote 6P needle growth. This highlights the robustness of MLG's interfacial properties against contamination and defects, albeit future work will be required to understand detailed dependencies on organic molecule species and substrate-MLG interactions.[2,13,14,22,29–33]

While 6P grows in a needle-type mode on MLG irrespective of PMMA residue and defect levels, the systematic variation of the 6P needle lengths correlates with the amount and distribution of PMMA left on the surface. Only short needles are present on strongly PMMA contaminated samples. In such a scenario, the 6P needles nucleate at graphene wrinkles and extend perpendicular to the wrinkle direction until they terminate at a PMMA contaminated area. This indicates that PMMA limits 6P molecular diffusion and/or attachment.[10] This is further corroborated by the comparably high nucleation density just at the wrinkles on the as transferred MLG (Figure 2a). Upon H_2 annealing, the PMMA is successively removed from the graphene basal plane (Figure 4a,b). The reduction of PMMA residuals results in less influence on 6P diffusion and attachment mechanisms, thus yielding longer needles. As the overall deposited 6P volume is kept constant in our experiments, the larger needle lengths result in the observed lower needle areal densities. In addition to the wrinkles, also the longer needles start to act as nucleation centers for additional 6P needles, and the 6P growth morphology on high temperature H_2 annealed CVD MLG approaches the highly crystalline characteristics of 6P needle structures on clean exfoliated graphene.[12,13]

In summary, we have systematically investigated the effects of transfer-induced PMMA residues and defects on the growth modes of the model organic semiconductor molecule 6P on CVD MLG. 6P grows in a flat-lying needle-type morphology on CVD MLG, irrespective of observed PMMA residue and graphene defect levels. This implies a surprising persistance of MLG in dominating interface properties even in the case of severe contamination or damage. 6P needles nucleate preferentially from wrinkles in the MLG. While PMMA residues do not have an impact on the growth mode of 6P, they severely restrict the length of the resulting 6P needles by limiting molecular diffusion/attachment. H_2 annealing prior to 6P deposition however recovers extended 6P needle growth, approaching the characteristics of 6P on clean exfoliated MLG. This underscores the importance of post-transfer cleaning processes for integration of MLG into organic electronics.

Acknowledgements

B.C.B acknowledges a College Research Fellowship from Hughes Hall, Cambridge. P.R.K. acknowledges the Lindemann Trust Fellowship. A.M. and G.R. acknowledge support by the Serbian MPNTR through Projects OI 171005 and III 45018. R.S.W. acknowledges a research fellowship from St. John's College, Cambridge. S.H. acknowledges funding from EPSRC (GRAPHTED, Grant No. EP/K016636/1). We want to thank Dr. Sarah M. Skoff (Vienna University of Technology, Austria) for fruitful discussions.

Figures

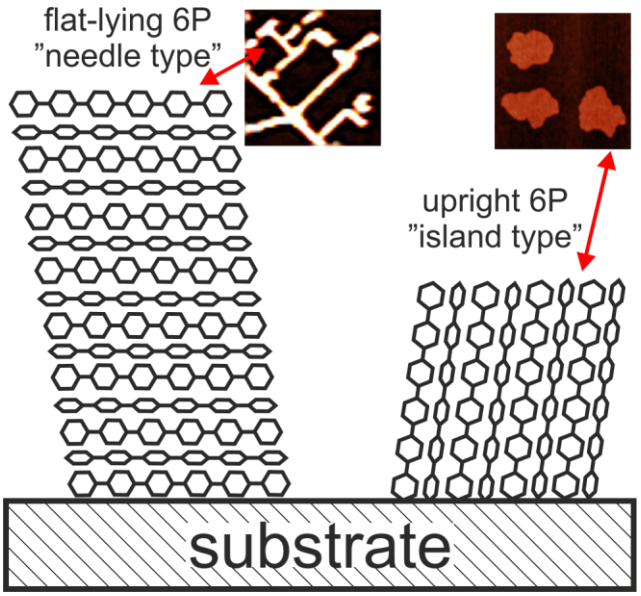

Figure 1. Schematic sketch of the two principal 6P growth morphologies: Flat-lying configuration forming "needles" (left) and upright configuration forming "islands" (right). The needles' long axes extend normal to the 6P molecular long axis (here normal to the page plane). Note that needles are typically comprised of multiple 6P layers and thus several tens of nm in height while islands are comprised of terraced 6P mounds with discrete heights corresponding to multiples of the 6P length of ~2.66 nm. At low coverages, usually only mono- or bi-layer 6P islands are observed.[12,13] The insets show corresponding atomic force microscopy (AFM) images of needle and island growth on exfoliated MLG[12,13] and amorphous carbon, respectively (1.75×1.75 μm^2, z-scale 10 nm, see also below).

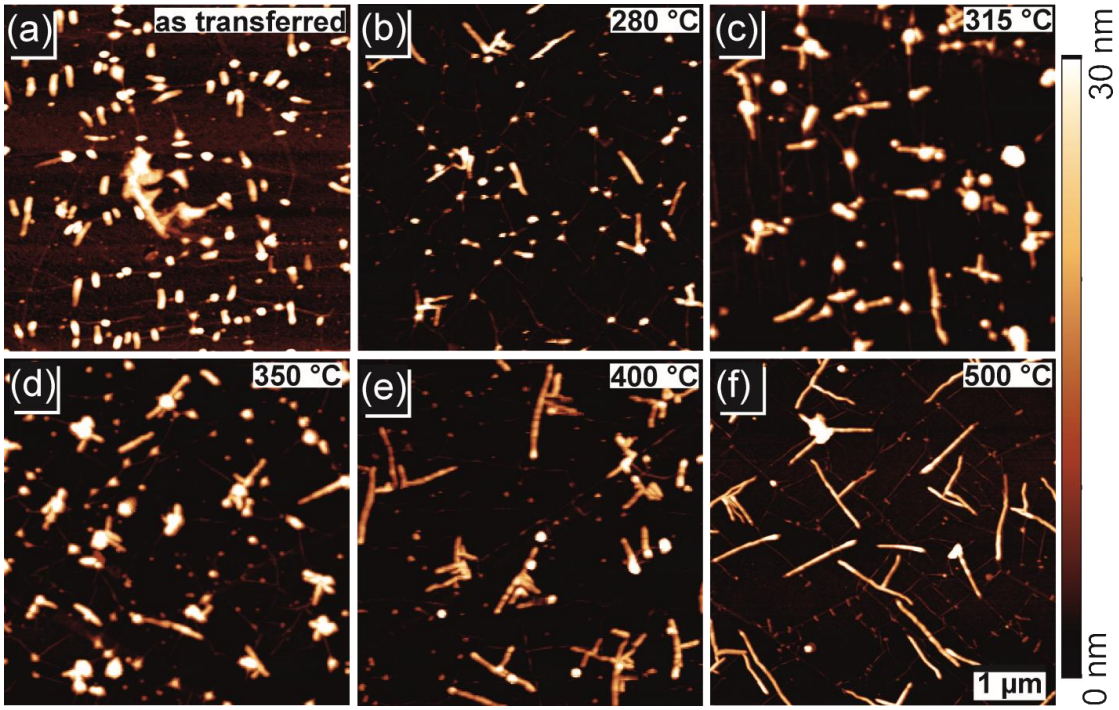

Figure 2. AFM topography images (5×5 µm^2) of 6P morphologies arising upon 6P deposition on PMMA-transferred CVD MLG which was H_2 annealed at varying temperatures prior to 6P deposition. The corresponding H_2 annealing temperatures are given in the right top corner of the images. To emphasize the MLG wrinkles, the same AFM data is plotted with a lower maximum z-scale in Supporting Figure S1.[59]

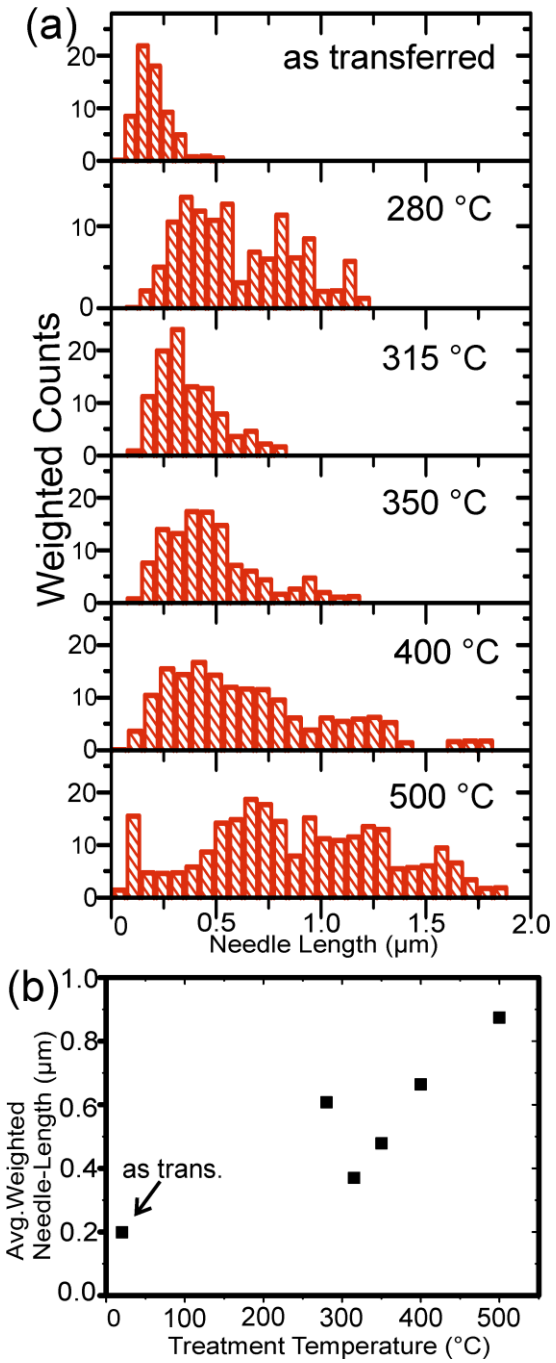

Figure 3. (a) 6P needle length distributions for CVD MLG samples that were H_2 annealed at different temperatures prior to 6P deposition. The histograms present needle-length-weighted needle counts over needle length. (For histogram data without length-weighting see Supporting Figure S2.[59]) (b) Average weighted needle lengths calculated from the histograms in (a). We note that for the 280 °C annealed sample it is difficult to distinguish needles from adjoining PMMA residuals since there these partly exhibit comparable heights and diameters as the 6P needles. As a result the corresponding distribution for 280 °C appears somewhat broadened and shifted to higher values.

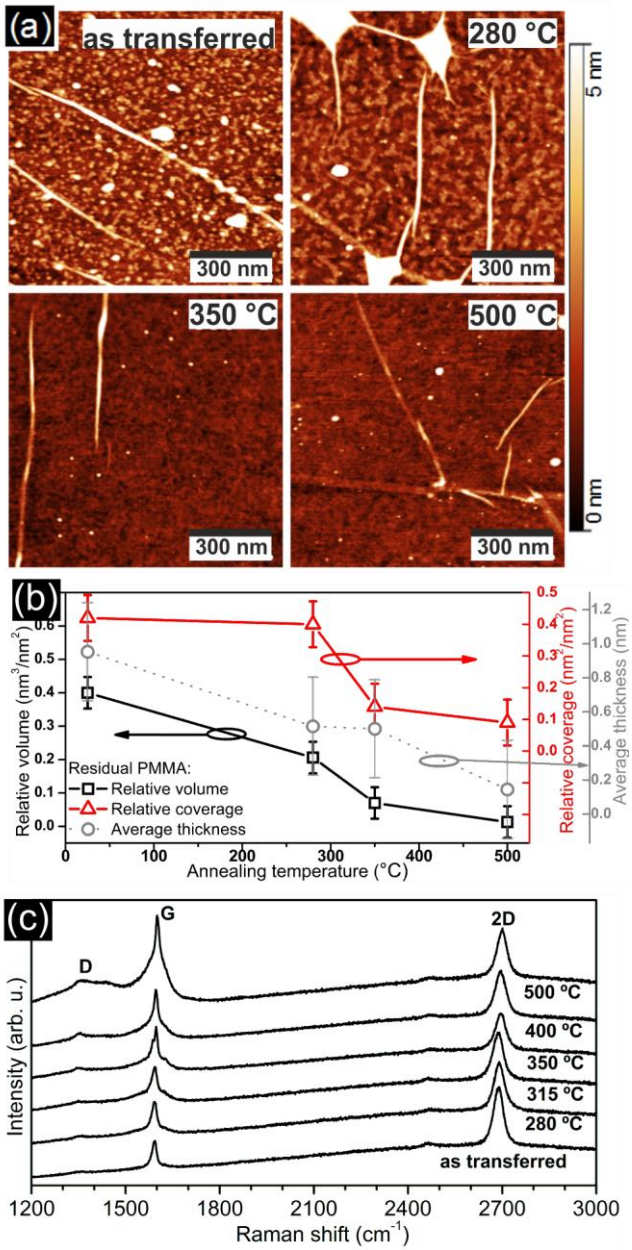

Figure 4. (a) 1×1 μm^2 AFM micrographs of PMMA-transferred CVD MLG which was H_2 annealed at varying temperatures. Note that the polygonal high features in the 280 °C scan with heights >5 nm are junctions of multiple MLG wrinkles coming together, see Supporting Figure S3[59] for the same data plotted on a larger z-scale. We note that areas with these polygonal features are not exclusive to the 280 °C sample but are observed in all CVD MLG samples. The 280 °C sample in fact mostly exhibits a MLG wrinkling morphology similar to the 25 °C, 350 °C and 500 °C scans i.e. without these polygonal features. This particular 280 °C scan is shown to illustrate the existence of these polygonal wrinkle junctions across our samples. Comparison of Figure 4a and Supporting Figure S3[59] also reveals that in

order to detect small PMMA contamination levels high resolution AFM scanning on a small z-scale has to be employed. (b) Relative volume, relative coverage (i.e. relative contact area of PMMA residues and MLG) and average thickness of residual PMMA as function of the H_2 annealing temperature (y-axes partly offset for readability). These quantifications of PMMA residue content were obtained via numerical height threshold analysis on AFM topography data.[59] (c) Corresponding Raman spectra showing the evolution of the characteristic MLG G and 2D bands and the defect related D band with H_2 annealing temperature.

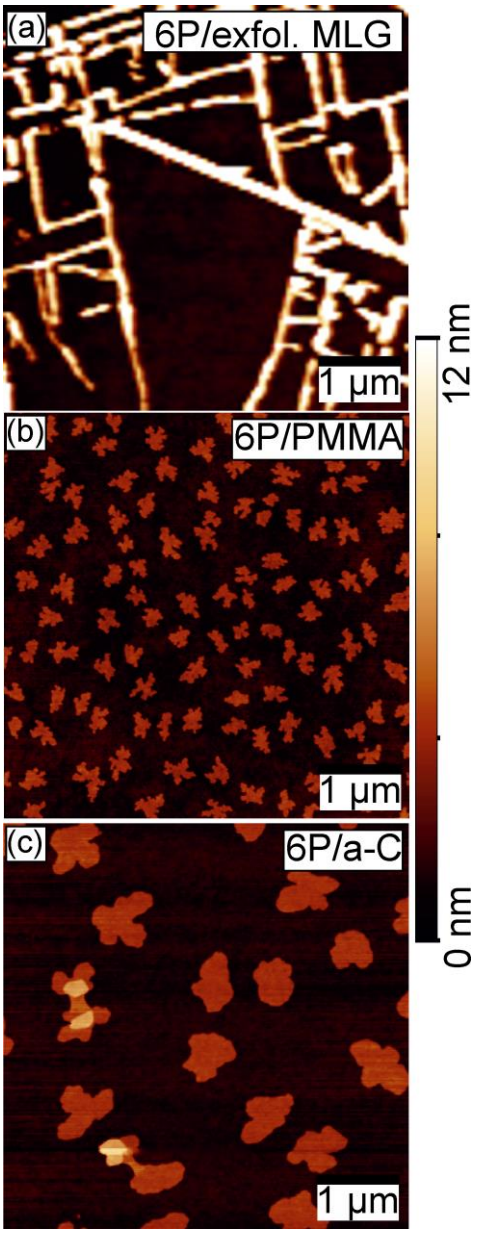

Figure 5. 5×5 µm^2 AFM micrographs of 6P deposited onto (a) exfoliated MLG (b) a spin-coated PMMA layer and (c) an a-C film. Comparison of (a) with (b) and (c) clearly reveals the different lateral 6P morphologies and 6P feature heights involved between needle (a) and island (b,c) growth.

References

[1] S. Pang, Y. Hernandez, X. Feng, and K. Müllen, Adv. Mater. **23**, 2779 (2011).
[2] W.H. Lee, J. Park, S.H. Sim, S. Lim, K.S. Kim, B.H. Hong, and K. Cho, J. Am. Chem. Soc. **133**, 4447 (2011).
[3] C.-H. Lee, T. Schiros, E.J.G. Santos, B. Kim, K.G. Yager, S.J. Kang, S. Lee, J. Yu, K. Watanabe, T. Taniguchi, J. Hone, E. Kaxiras, C. Nuckolls, and P. Kim, Adv. Mater. **26**, 2812 (2014).
[4] L. Gomez De Arco, Y. Zhang, C.W. Schlenker, K. Ryu, M.E. Thompson, and C. Zhou, ACS Nano **4**, 2865 (2010).
[5] M. He, J. Jung, F. Qiu, and Z. Lin, J. Mater. Chem. **22**, 24254 (2012).
[6] T. Sun, Z.L. Wang, Z.J. Shi, G.Z. Ran, W.J. Xu, Z.Y. Wang, Y.Z. Li, L. Dai, and G.G. Qin, Appl. Phys. Lett. **96**, (2010).
[7] T.-H. Han, Y. Lee, M.-R. Choi, S.-H. Woo, S.-H. Bae, B.H. Hong, J.-H. Ahn, and T.-W. Lee, Nat. Photonics **6**, 105 (2012).
[8] J. Meyer, P.R. Kidambi, B.C. Bayer, C. Weijtens, A. Kuhn, A. Centeno, A. Pesquera, A. Zurutuza, J. Robertson, and S. Hofmann, Sci. Rep. **4**, (2014).
[9] G. Hlawacek, F.S. Khokhar, R. van Gastel, B. Poelsema, and C. Teichert, Nano Lett. **11**, 333 (2011).
[10] G. Hlawacek, F.S. Khokar, R. van Gastel, C. Teichert, and B. Poelsema, IBM J. Res. Dev. **55**, 15 (2011).
[11] F.S. Khokhar, G. Hlawacek, R. Van Gastel, H.J. Zandvliet, C. Teichert, and B. Poelsema, Surf. Sci. **606**, 475 (2012).
[12] M. Kratzer, S. Klima, C. Teichert, B. Vasić, A. Matković, U. Ralević, and R. Gajić, J. Vac. Sci. Technol. B **31**, 04D114 (2013).
[13] M. Kratzer, S. Klima, C. Teichert, B. Vasić, A. Matković, M. Milićević, and R. Gajić, E-J. Surf. Sci. Nanotechnol. **12**, 31 (2014).
[14] F. Balzer, H.H. Henrichsen, M.B. Klarskov, T.J. Booth, R. Sun, J. Parisi, M. Schiek, and P. Bøggild, Nanotechnology **25**, 035602 (2014).
[15] Q.H. Wang and M.C. Hersam, Nat. Chem. **1**, 206 (2009).
[16] H. Huang, S. Chen, X. Gao, W. Chen, and A.T.S. Wee, ACS Nano **3**, 3431 (2009).
[17] H.Y. Mao, R. Wang, Y. Wang, T.C. Niu, J.Q. Zhong, M.Y. Huang, D.C. Qi, K.P. Loh, A.T.S. Wee, and W. Chen, Appl. Phys. Lett. **99**, 093301 (2011).
[18] I. Salzmann, A. Moser, M. Oehzelt, T. Breuer, X. Feng, Z.-Y. Juang, D. Nabok, R.G. Della Valle, S. Duhm, G. Heimel, A. Brillante, E. Venuti, I. Bilotti, C. Christodoulou, J. Frisch, P. Puschnig, C. Draxl, G. Witte, K. Müllen, and N. Koch, ACS Nano **6**, 10874 (2012).
[19] K. Xiao, W. Deng, J.K. Keum, M. Yoon, I.V. Vlassiouk, K.W. Clark, A.-P. Li, I.I. Kravchenko, G. Gu, E.A. Payzant, B.G. Sumpter, S.C. Smith, J.F. Browning, and D.B. Geohegan, J. Am. Chem. Soc. **135**, 3680 (2013).
[20] R. Addou and M. Batzill, Langmuir **29**, 6354 (2013).
[21] P. Järvinen, S.K. Hämäläinen, K. Banerjee, P. Häkkinen, M. Ijäs, A. Harju, and P. Liljeroth, Nano Lett. **13**, 3199 (2013).
[22] X. Liu, A. Grüneis, D. Haberer, A.V. Fedorov, O. Vilkov, W. Strupinski, and T. Pichler, J. Phys. Chem. C **117**, 3969 (2013).
[23] A. Riss, S. Wickenburg, L.Z. Tan, H.-Z. Tsai, Y. Kim, J. Lu, A.J. Bradley, M. Moreno Ugeda, K. Meaker, and K. Watanabe, ACS Nano (2014).
[24] W. Jung, D.-H. Oh, I. Song, H.-C. Shin, S.J. Ahn, Y. Moon, C.-Y. Park, and J.R. Ahn, Appl. Phys. Lett. **105**, (2014).
[25] J. MacLeod and F. Rosei, Small **10**, 1038 (2014).
[26] W. Chen, H. Huang, A. Thye, and S. Wee, Chem Commun 4276 (2008).
[27] J. Götzen, D. Käfer, C. Wöll, and G. Witte, Phys. Rev. B **81**, 085440 (2010).
[28] M. Chhikara, E. Pavlica, and G. Bratina, Surf. Sci. **609**, L5 (2013).
[29] H. Zhou, L. Zhang, J. Mao, G. Li, Y. Zhang, Y. Wang, S. Du, W.A. Hofer, and H.-J. Gao, Nano Res. **6**, 131 (2013).
[30] M. Chhikara, E. Pavlica, A. Matković, A. Beltaos, R. Gajić, and G. Bratina, Carbon **69**, 162 (2014).
[31] M. Chhikara, E. Pavlica, A. Matković, R. Gajić, and G. Bratina, Langmuir **30**, 11681 (2014).
[32] P.R. Kidambi, C. Ducati, B. Dlubak, D. Gardiner, R.S. Weatherup, M.-B. Martin, P. Seneor, H. Coles, and S. Hofmann, J. Phys. Chem. C **116**, 22492 (2012).
[33] P.R. Kidambi, B.C. Bayer, R. Blume, Z.-J. Wang, C. Baehtz, R.S. Weatherup, M.-G. Willinger, R. Schloegl, and S. Hofmann, Nano Lett. **13**, 4769 (2013).
[34] Y.-C. Lin, C.-C. Lu, C.-H. Yeh, C. Jin, K. Suenaga, and P.-W. Chiu, Nano Lett. **12**, 414 (2011).

[35] X. Liang, B.A. Sperling, I. Calizo, G. Cheng, C.A. Hacker, Q. Zhang, Y. Obeng, K. Yan, H. Peng, Q. Li, X. Zhu, H. Yuan, A.R. Hight Walker, Z. Liu, L. Peng, and C.A. Richter, ACS Nano **5**, 9144 (2011).
[36] A. Pirkle, J. Chan, A. Venugopal, D. Hinojos, C.W. Magnuson, S. McDonnell, L. Colombo, E.M. Vogel, R.S. Ruoff, and R.M. Wallace, Appl. Phys. Lett. **99**, 122108 (2011).
[37] N. Peltekis, S. Kumar, N. McEvoy, K. Lee, A. Weidlich, and G.S. Duesberg, Carbon **50**, 395 (2012).
[38] Y. Ahn, H. Kim, Y.-H. Kim, Y. Yi, and S.-I. Kim, Appl. Phys. Lett. **102**, 091602 (2013).
[39] A. Matković, U. Ralević, M. Chhikara, M.M. Jakovljević, D. Jovanović, G. Bratina, and R. Gajić, J. Appl. Phys. **114**, 093505 (2013).
[40] K. Kumar, Y.-S. Kim, and E.-H. Yang, Carbon **65**, 35 (2013).
[41] J.W. Suk, W.H. Lee, J. Lee, H. Chou, R.D. Piner, Y. Hao, D. Akinwande, and R.S. Ruoff, Nano Lett. **13**, 1462 (2013).
[42] A. Capasso, M. De Francesco, E. Leoni, T. Dikonimos, F. Buonocore, L. Lancellotti, E. Bobeico, M.S. Sarto, A. Tamburrano, G. De Bellis, and N. Lisi, Appl. Phys. Lett. **105**, 113101 (2014).
[43] M. Ishigami, J. Chen, W. Cullen, M. Fuhrer, and E. Williams, Nano Lett. **7**, 1643 (2007).
[44] Y. Dan, Y. Lu, N.J. Kybert, Z. Luo, and A.C. Johnson, Nano Lett. **9**, 1472 (2009).
[45] Z. Cheng, Q. Zhou, C. Wang, Q. Li, C. Wang, and Y. Fang, Nano Lett. **11**, 767 (2011).
[46] H. Yanagi and S. Okamoto, Appl. Phys. Lett. **71**, 2563 (1997).
[47] G. Leising, S. Tasch, C. Brandstatter, F. Meghdadi, G. Froyer, and L. Athouel, Adv. Mater. **9**, 33 (1997).
[48] A. Andreev, G. Matt, C.J. Brabec, H. Sitter, D. Badt, H. Seyringer, and N. Sariciftci, Adv. Mater. **12**, 629 (2000).
[49] G. Koller, S. Berkebile, J.R. Krenn, F.P. Netzer, M. Oehzelt, T. Haber, R. Resel, and M.G. Ramsey, Nano Lett. **6**, 1207 (2006).
[50] G. Hlawacek, P. Puschnig, P. Frank, A. Winkler, C. Ambrosch-Draxl, and C. Teichert, Science **321**, 108 (2008).
[51] C. Simbrunner, G. Hernandez-Sosa, F. Quochi, G. Schwabegger, C. Botta, M. Oehzelt, I. Salzmann, T. Djuric, A. Neuhold, R. Resel, M. Saba, A. Mura, G. Bongiovanni, A. Vollmer, N. Koch, and H. Sitter, ACS Nano **6**, 4629 (2012).
[52] F. Balzer and H. Rubahn, Adv. Funct. Mater. **15**, 17 (2005).
[53] S. Müllegger and A. Winkler, Surf. Sci. **600**, 1290 (2006).
[54] P. Frank, G. Hlawacek, O. Lengyel, A. Satka, C. Teichert, R. Resel, and A. Winkler, Surf. Sci. **601**, 2152 (2007).
[55] Z.-H. Wang, K. Kanai, K. Iketaki, Y. Ouchi, and K. Seki, Thin Solid Films **516**, 2711 (2008).
[56] T. Potocar, S. Lorbek, D. Nabok, Q. Shen, L. Tumbek, G. Hlawacek, P. Puschnig, C. Ambrosch-Draxl, C. Teichert, and A. Winkler, Phys. Rev. B **83**, 075423 (2011).
[57] G. Schwabegger, M. Oehzelt, I. Salzmann, F. Quochi, M. Saba, A. Mura, G. Bongiovanni, A. Vollmer, N. Koch, H. Sitter, and C. Simbrunner, Langmuir **29**, 14444 (2013).
[58] G. Hlawacek and C. Teichert, J. Phys. Condens. Matter **25**, 143202 (2013).
[59]See supplementary material at [URL will be inserted by AIP] for detailed description of methods, AFM data plotted at alternate z-scaling and additional Raman data. (n.d.).
[60] S. Lorbek, G. Hlawacek, and C. Teichert, Eur. Phys. J. Appl. Phys. **55**, 23902 (2011).
[61] J. Björk, F. Hanke, C.-A. Palma, P. Samori, M. Cecchini, and M. Persson, J. Phys. Chem. Lett. **1**, 3407 (2010).
[62] A.C. Ferrari and D.M. Basko, Nat. Nanotechnol. **8**, 235 (2013).
[63] R.S. Weatherup, C. Baehtz, B. Dlubak, B.C. Bayer, P.R. Kidambi, R. Blume, R. Schloegl, and S. Hofmann, Nano Lett. **13**, 4624 (2013).